


REVIEW

Open Access



Analysis of Vibration Characteristics of Electro-hydraulic Driven 3-UPS/S Parallel Stabilization Platform

Xiaoming Yuan^{1,2*} , Weiqi Wang^{1,2}, Haodong Pang^{1,2} and Lijie Zhang^{1,2}

Abstract

With the development of fluid-power transmission and control technology, electro-hydraulic-driven technology can significantly improve the load-carrying capacity, stiffness, and control accuracy of stabilization platforms. However, compared with mechanically driven platforms, the stiffness and damping of the fluid, as well as the coupling effect between the fluid and the structure need to be considered for electro-hydraulic-driven parallel stabilization platforms, making the modal and dynamic response characteristics of the mechanism more complex. With the aim of solving the aforementioned issues, we research the electro-hydraulic driven 3-UPS/S parallel stabilization platform considering the hinge stiffness. Moreover, the characteristic vibration equation of the mechanism is established using the virtual work principle. Subsequently, the variation characteristics of the natural frequency and the vibration response according to the position of the mechanism are analyzed based on the dynamic equation. Finally, the correctness of the model is verified by a modal test and Runge-Kutta methods. This study provides a theoretical basis for the dynamic design of electrohydraulic-driven parallel mechanisms.

Keywords Electro-hydraulic driven 3-UPS/S parallel stabilization platform, Kinetic equation, Vibration mode, Vibration response, Modal test

1 Introduction

A stabilization platform detects any position change of the equipment on it through a sensitive element, compensates for the deviation in the position of the equipment through attitude adjustment, and isolates the equipment from the influence of the environment to keep it relatively stable in inertial space [1–4]. According to the type of mechanism, a platform can be classified into a series or parallel stabilization platform [5, 6]. A series stabilization platform is simple to control and has a low design cost [7]. Thus, they

are widely used in fields such as laser positioning, satellite communication, missile guidance, and for unmanned reconnaissance aircrafts. In contrast, a parallel stabilization platform is driven by multi-axis coupling and has the characteristics of a strong bearing capacity and high stiffness and therefore has a wide range of application scenarios in high-precision operations such as weapon launches and maritime rescues [8–11]. By adopting the electro-hydraulic driven platform with the advantages of its high power/weight ratio, fast response speed and small cumulative error, however, the motion control accuracy of the stabilization platform can be greatly improved [12–15].

Mechanical vibrations can cause dynamic deformation and relative motion of platform structures, thereby increasing the stress and fatigue loads on various components of the platform. This subsequently affects the stability, control accuracy, and service life of the platform, and in severe cases, can even lead to structural

*Correspondence:

Xiaoming Yuan
xiaomingbingbing@163.com

¹ Hebei Key Laboratory of Heavy Machinery Fluid Power Transmission and Control, Yanshan University, Qinhuangdao 066004, China

² Key Laboratory of Advanced Forging & Stamping Technology and Science, Ministry of Education, Yanshan University, Qinhuangdao 066004, China

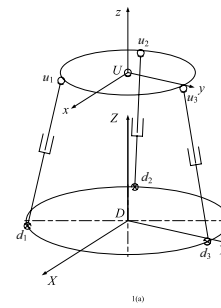
damage [16–18]. Therefore, to further improve the performance of parallel stabilization platforms, it is important to study their vibration characteristics [19, 20]. There are three methods for studying the vibration characteristics: the simulation analysis method [21–23], theoretical analysis method [24] and experimental analysis method [25]. The simulation analysis method is used to analyze the vibration characteristics after solving the characteristic value of the finite element analysis of the structure [26–28]. Therefore, it is widely used to analyze the vibration characteristics of complex mechanical systems. The experimental analysis method is used to estimate the modal parameters of the mechanism through the frequency response function measured in practice and it is also used to verify the results of the simulation and theoretical analysis [29, 30]. The theoretical analysis method is used to analyze the vibration characteristics based on the dynamic equation and the analytical solution of the vibration response [31, 32]. It can quantitatively analyze the vibration characteristics of a mechanism and is a common method for the further study of mechanical vibrations. However, during the process of dynamic modeling, previous studies did not consider the influence of flexible stiffness [33, 34]. Moreover, with the development of the finite element method, hinge stiffness has gradually been studied, which has also led to a low computational efficiency with regards to dynamic calculations [35]. Additionally, the variation characteristics of the natural frequency and vibration response with respect to the position of the mechanism have not yet been studied.

Therefore, taking an electro-hydraulic driven 3-UPS/S parallel stabilization platform as research object, its mechanical-hydraulic coupling dynamic equation is established considering the hinge stiffness. Subsequently, the modal and resonant characteristics of the mechanism are studied. The theoretical model is verified through numerical simulations and modal tests. This study provides a theoretical basis for dynamic modal analysis and resonance research on parallel mechanisms.

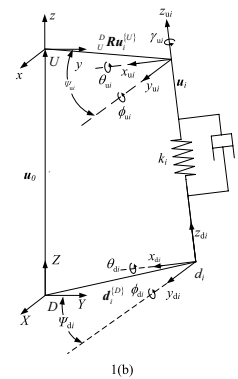
2 Kinematic Analysis of Electro-hydraulic Driven 3-UPS/S Parallel Stabilization Platform

2.1 Position Analysis of Electro-hydraulic Driven 3-UPS/S Parallel Stabilization Platform

As shown in Figure 1(a), an electro-hydraulic driven 3-UPS/S parallel stabilization platform consists of a moving platform, supporting branch chain, static platform, and three driving branches. The coordinate system $U-xyz$ is the fixed coordinate system of the moving platform and the coordinate system $D-XYZ$ is the fixed coordinate system of the static platform.



(a) Schematic diagram of electro-hydraulic driven 3-UPS/S parallel stabilization platform



(b) Drive chain position vector diagram

Figure 1 Coordinate system of electro-hydraulic 3-UPS/S parallel stabilization platform

As shown in Figure 1(b), the local coordinate system $d_i-x_{di}y_{di}z_{di}$ is established at the center of the universal joint, established at the center of the spherical hinge. Axes z_{di} and axis z_{ui} are in the same direction as the unit-direction vector e_i of the driving branch. The rotation angles of the universal joint about axis x_{di} and axis y_{di} are, respectively, θ_{di} and ϕ_{di} ; the rotation angles of the spherical hinge about axis x_{ui} , axis y_{ui} and axis z_{ui} are, respectively, θ_{ui} , ϕ_{ui} , γ_{ui} ; ψ_{di} , ψ_{ui} are the installation angles of the universal joint and the spherical hinge, respectively, which are determined by the platform structure.

The closed-loop equation of the drive chain can be expressed as:

$$l_i e_i = {}^D_U R u_i^{\{U\}} - d_i^{\{D\}} + u_0 + u, \tag{1}$$

where l_i is the length of the drive chain; e_i is the unit direction vector of the drive chain; ${}^D_U R$ is the rotation transformation matrix between the coordinate system $U-xyz$ and the coordinate system $D-XYZ$; $u_i^{\{U\}}$ is the vector from the center of the spherical hinge to the

origin of the coordinate system $U-xyz$; $\mathbf{d}_i^{(D)}$ is the vector from the center of the universal joint to the origin of the coordinate system $D-XYZ$; \mathbf{u}_0 is the initial displacement vector of the coordinate system $U-xyz$ to the coordinate system $D-XYZ$; \mathbf{u} is the displacement vector of the coordinate system $U-xyz$ to the coordinate system $D-XYZ$.

Thus, the equation for the drive chain length can be expressed as:

$$l_i = \left\| {}^D_U \mathbf{R} \mathbf{u}_i^{(U)} - \mathbf{d}_i^{(D)} + \mathbf{u}_0 + \mathbf{u} \right\|. \tag{2}$$

The centroid position of the lower connecting rod of the drive chain can be expressed as:

$$\mathbf{p}_{gi} = \mathbf{d}_i^{(D)} + q_i \mathbf{e}_i, \tag{3}$$

where \mathbf{p}_{gi} is the position vector of the lower connecting rod centroid and q_i is the distance between the centroid of the lower connecting rod and the center of the universal joint.

The rotation transformation matrix between the local coordinate system $d_i-x_{di}y_{di}z_{di}$ and the coordinate system $D-XYZ$ can be expressed as:

$${}^D_{d_i} \mathbf{R} = \mathbf{R}(\psi_{di}, z_{di}) \mathbf{R}(\phi_{di}, y_{di}) \mathbf{R}(\theta_{di}, x_{di}). \tag{4}$$

Because axis z_{di} is in the same direction as the unit direction vector \mathbf{e}_p , z_{di} can be expressed as:

$$\begin{bmatrix} e_{xi} \\ e_{yi} \\ e_{zi} \end{bmatrix} = \begin{bmatrix} \sin \psi_{di} \sin \theta_{di} + \cos \psi_{di} \sin \phi_{di} \cos \theta_{di} \\ \sin \psi_{di} \sin \phi_{di} \cos \theta_{di} - \cos \psi_{di} \cos \theta_{di} \\ \cos \phi_{di} \cos \theta_{di} \end{bmatrix}. \tag{5}$$

Thus, the rotation angle of the universal joint is:

$$\begin{cases} \phi_{di} = \arctan\left(\frac{e_{xi} \cos \psi_{di} + e_{yi} \sin \psi_{di}}{e_{zi}}\right), \\ \theta_{di} = -\arcsin(e_{yi} \cos \psi_{di} - e_{xi} \sin \psi_{di}). \end{cases} \tag{6}$$

If the local coordinate systems $d_i-x_{di}y_{di}z_{di}$ and $u_i-x_{ui}y_{ui}z_{ui}$ have the same direction, the rotation transformation matrix ${}^D_{u_i} \mathbf{R}$ between the local coordinate system $u_i-x_{ui}y_{ui}z_{ui}$ and the coordinate system $D-XYZ$ can be obtained from Eq. (4). Thus, the rotation angle of the spherical hinge is:

$$\begin{cases} \phi_{ui} = \arctan\left(\frac{(\mathbf{R}_{Fi})_{1,3}}{(\mathbf{R}_{Fi})_{3,3}}\right), \\ \theta_{ui} = -\arcsin((\mathbf{R}_{Fi})_{2,3}), \\ \gamma_{ui} = \arctan\left(\frac{(\mathbf{R}_{Fi})_{2,1}}{(\mathbf{R}_{Fi})_{2,2}}\right), \end{cases} \tag{7}$$

where $\mathbf{R}_{Fi} = \mathbf{R}(\psi_{ui}, z_{ui}) {}^D_U \mathbf{R} {}^T_{u_i} \mathbf{R}^T$.

2.2 Velocity Analysis of Electro-hydraulic Driven 3-UPS/S Parallel Stabilization Platform

By solving the first derivative with respect to time in Eq. (1), the velocity equation of the drive chain can be expressed as:

$$\dot{l}_i \mathbf{e}_i + l_i \boldsymbol{\omega}_{zi} \times \mathbf{e}_i = \boldsymbol{\omega}_u \times {}^D_U \mathbf{R} \mathbf{u}_i^{(U)}, \tag{8}$$

where $\boldsymbol{\omega}_{zi}$ is the angular velocity of the drive chain and $\boldsymbol{\omega}_u$ is that of the moving platform.

Then, the Jacobian matrix between the drive chain and the moving platform is:

$$\mathbf{J}_u = \begin{bmatrix} {}^D_U \mathbf{R} \mathbf{u}_1^{(U)} \times \mathbf{e}_1 \\ {}^D_U \mathbf{R} \mathbf{u}_2^{(U)} \times \mathbf{e}_2 \\ {}^D_U \mathbf{R} \mathbf{u}_3^{(U)} \times \mathbf{e}_3 \end{bmatrix}. \tag{9}$$

By multiplying both sides of Eq. (8) by the unit direction vector \mathbf{e}_p and expressing the result in the local coordinate system $d_i-x_{di}y_{di}z_{di}$, the result can be shown as follows:

$$\begin{bmatrix} \left(\omega_z^{(d_i)}\right)_x \\ \left(\omega_z^{(d_i)}\right)_y \\ 0 \end{bmatrix} = \frac{1}{l_i} \begin{bmatrix} -\left(v_{ui}^{(d_i)}\right)_y \\ \left(v_{ui}^{(d_i)}\right)_x \\ 0 \end{bmatrix}, \tag{10}$$

where $v_{ui}^{(d_i)}$ represents the center velocity of the spherical hinge in the local coordinate system $d_i-x_{di}y_{di}z_{di}$.

The angular velocity of the drive chain is generated by the rotation of the universal joint, so the angular velocity of the drive chain rotation can be expressed in the local coordinate system $d_i-x_{di}y_{di}z_{di}$ as:

$$\boldsymbol{\omega}_z = \dot{\phi}_{di} \mathbf{y}_{di} + \dot{\theta}_{di} \mathbf{x}_{di}. \tag{11}$$

By representing the vector in Eq. (9) in the local coordinate system $d_i-x_{di}y_{di}z_{di}$, Eq. (9) can be expressed as:

$$\begin{aligned} \boldsymbol{\omega}_z^{(d_i)} &= \dot{\phi}_{di} \mathbf{R}(\theta_{di}, x_{di})^T \mathbf{R}(\phi_{di}, y_{di})^T (0 \ 1 \ 0)^T \\ &+ \dot{\theta}_{di} \mathbf{R}(\theta_{di}, x_{di})^T (1 \ 0 \ 0)^T \\ &\approx (\dot{\theta}_{di} \ \dot{\phi}_{di} \ 0)^T. \end{aligned} \tag{12}$$

By combining Eqs. (10)–(12), the angular velocity of the universal joint can be expressed as:

$$\begin{cases} \dot{\phi}_{di} = -\frac{1}{l_i} \left(\frac{d_i}{U} \mathbf{R}\right)_{:,2} \cdot \left(\boldsymbol{\omega}_u \times {}^D_U \mathbf{R} \mathbf{u}_i^{(U)}\right), \\ \dot{\theta}_{di} = \frac{1}{l_i} \left(\frac{d_i}{U} \mathbf{R}\right)_{:,1} \cdot \left(\boldsymbol{\omega}_u \times {}^D_U \mathbf{R} \mathbf{u}_i^{(U)}\right). \end{cases} \tag{13}$$

Then, the Jacobian matrix of the universal joint is:

$$J_{fd} = \begin{bmatrix} -\frac{1}{l_1} \begin{pmatrix} d_1 \\ U \end{pmatrix} \mathbf{R} \Big|_{:,2} \cdot \left(\boldsymbol{\omega}_u \times \frac{D}{U} \mathbf{R} \mathbf{u}_1^{(U)} \right) \\ -\frac{1}{l_2} \begin{pmatrix} d_2 \\ U \end{pmatrix} \mathbf{R} \Big|_{:,2} \cdot \left(\boldsymbol{\omega}_u \times \frac{D}{U} \mathbf{R} \mathbf{u}_2^{(U)} \right) \\ -\frac{1}{l_3} \begin{pmatrix} d_3 \\ U \end{pmatrix} \mathbf{R} \Big|_{:,2} \cdot \left(\boldsymbol{\omega}_u \times \frac{D}{U} \mathbf{R} \mathbf{u}_3^{(U)} \right) \end{bmatrix}, \quad (14)$$

$$J_{xd} = \begin{bmatrix} \frac{1}{l_1} \begin{pmatrix} d_1 \\ U \end{pmatrix} \mathbf{R} \Big|_{:,2} \cdot \left(\boldsymbol{\omega}_u \times \frac{D}{U} \mathbf{R} \mathbf{u}_1^{(U)} \right) \\ \frac{1}{l_2} \begin{pmatrix} d_2 \\ U \end{pmatrix} \mathbf{R} \Big|_{:,2} \cdot \left(\boldsymbol{\omega}_u \times \frac{D}{U} \mathbf{R} \mathbf{u}_2^{(U)} \right) \\ \frac{1}{l_3} \begin{pmatrix} d_3 \\ U \end{pmatrix} \mathbf{R} \Big|_{:,2} \cdot \left(\boldsymbol{\omega}_u \times \frac{D}{U} \mathbf{R} \mathbf{u}_3^{(U)} \right) \end{bmatrix}. \quad (15)$$

Similarly, considering the motion transmission relationship between the spherical hinge and the moving platform, the angular velocity of the drive chain can be expressed as:

$$\boldsymbol{\omega}_z = \boldsymbol{\omega}_u + \dot{\phi}_{ui} \mathbf{y}_{di} + \dot{\theta}_{ui} \mathbf{x}_{ui} + \dot{\gamma}_{ui} \mathbf{z}_{ui}. \quad (16)$$

By representing the vector in Eq. (14) in the local coordinate system $u_i-x_{ui}y_{ui}z_{ui}$, Eq. (14) can be expressed as follows:

$$\begin{aligned} \boldsymbol{\omega}_z^{(u_i)} &= \boldsymbol{\omega}_u^{(u_i)} + \dot{\gamma}_{ui} \mathbf{R}(\gamma_{ui}, z_{ui})^T (0 \ 0 \ 1)^T \\ &+ \dot{\phi}_{ui} \mathbf{R}(\gamma_{ui}, z_{ui})^T \mathbf{R}(\theta_{ui}, x_{ui})^T \mathbf{R}(\phi_{ui}, y_{ui})^T (0 \ 1 \ 0)^T \\ &+ \dot{\theta}_{ui} \mathbf{R}(\gamma_{ui}, z_{ui})^T \mathbf{R}(\theta_{ui}, x_{ui})^T (1 \ 0 \ 0)^T \\ &\approx \boldsymbol{\omega}_u^{(u_i)} + (\dot{\phi}_{ui} \ \dot{\theta}_{ui} \ \dot{\gamma}_{ui})^T. \end{aligned} \quad (17)$$

By combining Eq. (11) and Eq. (17), the angular velocity of the spherical hinge can be expressed as:

$$\begin{cases} \dot{\phi}_{ui} = -\frac{1}{l_i} \begin{pmatrix} d_i \\ U \end{pmatrix} \mathbf{R} \Big|_{:,2} \cdot \left(\boldsymbol{\omega}_u \times \frac{D}{U} \mathbf{R} \mathbf{u}_i^{(U)} \right) - \begin{pmatrix} D \\ u_i \end{pmatrix} \mathbf{R} \Big|_{:,1} \cdot \boldsymbol{\omega}_u, \\ \dot{\theta}_{ui} = \frac{1}{l_i} \begin{pmatrix} d_i \\ U \end{pmatrix} \mathbf{R} \Big|_{:,1} \cdot \left(\boldsymbol{\omega}_u \times \frac{D}{U} \mathbf{R} \mathbf{u}_i^{(U)} \right) - \begin{pmatrix} D \\ u_i \end{pmatrix} \mathbf{R} \Big|_{:,2} \cdot \boldsymbol{\omega}_u, \\ \dot{\gamma}_{ui} = \frac{1}{l_i} \begin{pmatrix} d_i \\ U \end{pmatrix} \mathbf{R} \Big|_{:,3} \cdot \boldsymbol{\omega}_u. \end{cases} \quad (18)$$

Thus, the Jacobian matrix of the spherical hinge can be expressed as:

$$J_{gu} = \begin{bmatrix} -\begin{pmatrix} D \\ u_i \end{pmatrix} \mathbf{R} \Big|_{:,3}^T \\ -\begin{pmatrix} D \\ u_i \end{pmatrix} \mathbf{R} \Big|_{:,1}^T \\ -\begin{pmatrix} D \\ u_i \end{pmatrix} \mathbf{R} \Big|_{:,2}^T \end{bmatrix}, \quad (19)$$

$$J_{fu} = \begin{bmatrix} -\frac{1}{l_1} \begin{pmatrix} d_1 \\ U \end{pmatrix} \mathbf{R} \Big|_{:,2} \cdot \left(\boldsymbol{\omega}_u \times \frac{D}{U} \mathbf{R} \mathbf{u}_1^{(U)} \right)^T - \begin{pmatrix} D \\ u_i \end{pmatrix} \mathbf{R} \Big|_{:,1}^T \\ -\frac{1}{l_2} \begin{pmatrix} d_1 \\ U \end{pmatrix} \mathbf{R} \Big|_{:,2} \cdot \left(\boldsymbol{\omega}_u \times \frac{D}{U} \mathbf{R} \mathbf{u}_1^{(U)} \right)^T - \begin{pmatrix} D \\ u_i \end{pmatrix} \mathbf{R} \Big|_{:,1}^T \\ -\frac{1}{l_3} \begin{pmatrix} d_1 \\ U \end{pmatrix} \mathbf{R} \Big|_{:,2} \cdot \left(\boldsymbol{\omega}_u \times \frac{D}{U} \mathbf{R} \mathbf{u}_1^{(U)} \right)^T - \begin{pmatrix} D \\ u_i \end{pmatrix} \mathbf{R} \Big|_{:,1}^T \end{bmatrix}, \quad (20)$$

$$J_{xu} = \begin{bmatrix} -\frac{1}{l_1} \begin{pmatrix} d_1 \\ U \end{pmatrix} \mathbf{R} \Big|_{:,1} \cdot \left(\boldsymbol{\omega}_u \times \frac{D}{U} \mathbf{R} \mathbf{u}_1^{(U)} \right)^T - \begin{pmatrix} D \\ u_i \end{pmatrix} \mathbf{R} \Big|_{:,2}^T \\ -\frac{1}{l_2} \begin{pmatrix} d_1 \\ U \end{pmatrix} \mathbf{R} \Big|_{:,1} \cdot \left(\boldsymbol{\omega}_u \times \frac{D}{U} \mathbf{R} \mathbf{u}_1^{(U)} \right)^T - \begin{pmatrix} D \\ u_i \end{pmatrix} \mathbf{R} \Big|_{:,2}^T \\ -\frac{1}{l_3} \begin{pmatrix} d_1 \\ U \end{pmatrix} \mathbf{R} \Big|_{:,1} \cdot \left(\boldsymbol{\omega}_u \times \frac{D}{U} \mathbf{R} \mathbf{u}_1^{(U)} \right)^T - \begin{pmatrix} D \\ u_i \end{pmatrix} \mathbf{R} \Big|_{:,2}^T \end{bmatrix}. \quad (21)$$

By solving the first derivative with respect to time in Eq. (3), the result can be shown as follows:

$$\dot{\mathbf{p}}_{gi}^{\{d_i\}} = q_i \left(\boldsymbol{\omega}_z^{\{d_i\}} \times \mathbf{e}_i \right) = q_i \left(\dot{\phi}_{di} \ \dot{\theta}_{di} \ 0 \right)^T. \quad (22)$$

Combining Eq. (13) and Eq. (22), the Jacobian matrix of the lower connecting rod is:

$$J_{gi} = \begin{bmatrix} \frac{q_i}{l_i} \left(\left(\boldsymbol{\omega}_u \times \frac{D}{U} \mathbf{R} \mathbf{u}_i^{(U)} \right) \begin{pmatrix} d_i \\ U \end{pmatrix} \mathbf{R} \Big|_{:,2} \right)^T \\ -\frac{q_i}{l_i} \left(\left(\boldsymbol{\omega}_u \times \frac{D}{U} \mathbf{R} \mathbf{u}_i^{(U)} \right) \begin{pmatrix} d_i \\ U \end{pmatrix} \mathbf{R} \Big|_{:,1} \right)^T \\ \mathbf{0}^{1 \times 3} \end{bmatrix}. \quad (23)$$

Similarly, the Jacobian matrix of the upper connecting rod is:

$$J_{hi} = \begin{bmatrix} \frac{h_i}{l_i} \left(\left(\boldsymbol{\omega}_u \times \frac{D}{U} \mathbf{R} \mathbf{u}_i^{(U)} \right) \begin{pmatrix} d_i \\ U \end{pmatrix} \mathbf{R} \Big|_{:,2} \right)^T \\ -\frac{h_i}{l_i} \left(\left(\boldsymbol{\omega}_u \times \frac{D}{U} \mathbf{R} \mathbf{u}_i^{(U)} \right) \begin{pmatrix} d_i \\ U \end{pmatrix} \mathbf{R} \Big|_{:,1} \right)^T \\ \mathbf{0}^{1 \times 3} \end{bmatrix}, \quad (24)$$

where h_i is the distance between the centroid of the lower connecting rod and the center of the universal joint.

2.3 Dynamic Equation of Electro-hydraulic Driven 3-UPS/S Parallel Stabilization Platform

To derive the dynamic equation of an electro-hydraulic driven 3-UPS/S parallel stabilization platform, the following assumptions were made:

- (1) Errors in the processing and assembly processes were ignored.
- (2) The force of the drive chain on the moving platform was equivalent to the spring force along the expansion direction of the drive chain.
- (3) The passive joints of the mechanism adopted a ball-and-socket structure with rolling balls for point contact. Universal joints utilized needle-roller bearings. Therefore, friction at the passive joints of the mechanism was ignored.

The friction at the hydraulic cylinder in the mechanism is primarily manifested in the form of the viscous shear resistance of the hydraulic oil. Therefore, a fluid viscous damping coefficient was introduced during the process of

establishing the equation. According to the virtual work principle, the virtual power acting on each component of the mechanism can be calculated as follows:

$$C = J_u^T c J_u, \quad (29)$$

$$\begin{aligned} \delta p = & \left(f_u - k \Delta l - c \dot{l} \right) \cdot \delta l + \left(-I_u \dot{\omega}_u - \omega_u \times I_u \omega_u \right) \cdot \delta \omega_u \\ & + \left(-k_{xd} \Delta \theta_d \right) \cdot \delta \dot{\theta}_d + \left(-k_{fd} \Delta \psi_d \right) \cdot \delta \dot{\psi}_d + \left(-k_{xu} \Delta \theta_u \right) \cdot \delta \dot{\theta}_u \\ & + \sum_{i=1}^3 \left(-m_{gi} \ddot{p}_{gi}^{\{di\}} \cdot \delta \dot{p}_{gi}^{\{di\}} + \left(-I_{gi}^{\{di\}} \dot{\omega}_{gi}^{\{di\}} - \omega_{gi}^{\{di\}} \times I_{gi}^{\{di\}} \omega_{gi}^{\{di\}} \right) \cdot \delta \omega_{gi}^{\{di\}} \right) \\ & + \sum_{i=1}^3 \left(-m_{hi} \ddot{p}_{hi}^{\{di\}} \cdot \delta \dot{p}_{hi}^{\{di\}} + \left(-I_{hi}^{\{di\}} \dot{\omega}_{hi}^{\{di\}} - \omega_{hi}^{\{di\}} \times I_{hi}^{\{di\}} \omega_{hi}^{\{di\}} \right) \cdot \delta \omega_{hi}^{\{di\}} \right) \\ & + \left(-k_{fu} \Delta \psi_u \right) \cdot \delta \dot{\psi}_u + \left(-k_{gu} \Delta \gamma_u \right) \cdot \delta \dot{\gamma}_u = 0, \end{aligned} \quad (25)$$

where f_u is the force matrix on the moving platform; k is the stiffness matrix of the drive chain; c is the damping matrix of the drive chain; I_u is the inertia matrix of the moving platform; ω_u is the angular velocity of the moving platform; m_{gi} is the mass of the lower connecting rod; $p_{gi}^{\{di\}}$ is the displacement vector of the lower connecting rod; $I_{gi}^{\{di\}}$ is the inertia matrix of the lower connecting rod; $\omega_{gi}^{\{di\}}$ is the angular velocity of the lower connecting rod; m_{hi} is the mass of the upper connecting rod; $p_{hi}^{\{di\}}$ is the displacement vector of the upper connecting rod; $I_{hi}^{\{di\}}$ is the inertia matrix of the upper connecting rod; $\omega_{hi}^{\{di\}}$ is the angular velocity of the upper connecting rod.

By ignoring the Coriolis and centrifugal forces, Eq. (25) can be simplified as follows:

$$\begin{aligned} & \left(f_u - k J_u x - c J_u \dot{x} \right) \delta \dot{x} - \left(k_{xu} J_{xu} x \right)^T J_{xu} \delta \dot{x} \\ & - \left(k_{xd} J_{xd} x \right)^T J_{xd} \delta \dot{x} - \left(k_{fd} J_{fd} x \right)^T J_{fd} \delta \dot{x} \\ & - \left(k_{fu} J_{fu} x \right)^T J_{fu} \delta \dot{x} - \left(k_{gu} J_{gu} x \right)^T J_{gu} \delta \dot{x} \\ & - \sum_{i=1}^3 \left(I_{gi} \omega_{gi} J_{gi} + I_{hi} \omega_{hi} J_{hi} \right) \delta \dot{x} = 0, \end{aligned} \quad (26)$$

where $\dot{x} = \omega_u^T$.

The components of ω_u are independent because the generalized coordinates are independent. Therefore, the coefficient should be equal to zero. The explicit dynamic equation for this mechanism is as follows:

$$M \ddot{x} + C \dot{x} + K x = 0, \quad (27)$$

where

$$M = I_u + \sum_{i=1}^3 \left(J_{gi}^T I_{gi} J_{gi} + J_{hi}^T I_{hi} J_{hi} \right), \quad (28)$$

$$\begin{aligned} K = & J_u^T k J_u + J_{\theta d}^T k_{\theta d} J_{\theta d} + J_{\psi d}^T k_{\psi d} J_{\psi d} \\ & + J_{\theta u}^T k_{\theta u} J_{\theta u} + J_{\psi u}^T k_{\psi u} J_{\psi u} + J_{\gamma u}^T k_{\gamma u} J_{\gamma u}. \end{aligned} \quad (30)$$

3 Free Vibration Analysis of Electro-hydraulic Driven 3-UPS/S Parallel Stabilization Platform

3.1 Modal Analysis of Electro-hydraulic Driven 3-UPS/S Parallel Stabilization Platform in Fixed Posture

The structural parameters of the electro-hydraulic driven 3-UPS/S parallel stabilization platform are listed in Table 1.

Based on the parameters shown in Table 1, the modal and natural frequencies of the platform in the initial position $\alpha=0^\circ$, $\beta=0^\circ$, $\gamma=28^\circ$ and the random position $\alpha=10^\circ$, $\beta=10^\circ$, $\gamma=28^\circ$ are calculated, and the results are shown in Tables 2 and 3.

After analyzing the data in Tables 2 and 3, the following conclusions can be drawn:

- (1) At the initial position, the natural frequency in the deflection direction was at the minimum, and the natural frequencies in the directions of the rotation and pitch were approximately equal.
- (2) There is a certain coupling relationship between the vibration responses in the pitching and rotation directions; however, the coupling relationship between them and the deflection direction is small.
- (3) By changing the position of the mechanism, the coupling of the vibration response in every direction was enhanced, and the natural frequencies of each order changed. This is because the Jacobian matrix of the mechanism changed and affected its mass and stiffness matrices.
- (4) When the position of the mechanism changed, the natural frequencies of each order changed differ-

Table 1 Structural parameters of electro-hydraulic driven 3-UPS/S parallel stabilization platform

Parameter name	Parameter value
Rotational inertia of the moving platform I_u (kg·m ²)	diag [3.74 3.76 7.72]
Rotational inertia of the lower connecting rod I_g (kg·m ²)	diag [0.96 0.96 0.0506]
Rotational inertia of the upper connecting rod I_h (kg·m ²)	diag [0.19 0.19 0.0069]
Radius of the moving platform r_u (m)	0.38
Radius of the static platform r_d (m)	0.51
Mass of the moving platform m_u (kg)	65.703
Mass of the lower connecting rod m_g (kg)	20.604
Mass of the upper connecting rod m_h (kg)	4.263
Piston diameter of the hydraulic cylinder d_1 (m)	0.04
Piston rod diameter of the hydraulic cylinder d_2 (m)	0.025
bulk modulus of oil E (Pa)	1180×10^{-6}
Oil density ρ (kg/m ³)	900
Stiffness value of universal joint in rotation direction around axis x_{dj} , k_{xd} (N·m/rad)	72.07
Stiffness value of universal joint in rotation direction around axis y_{dj} , k_{yd} (N·m/rad)	72.07
Stiffness value of spherical hinge in rotation direction around axis x_{ui} , k_{xu} (N·m/rad)	51.15
Stiffness value of spherical hinge in rotation direction around axis y_{ui} , k_{yu} (N·m/rad)	62.79
Stiffness value of spherical hinge in rotation direction around axis z_{ui} , k_{zu} (N·m/rad)	64
viscous damping coefficient c (N·m/s)	1620

Table 2 Natural frequency and vibration mode at initial position

Order of natural frequency	First order natural frequency	Second order natural frequency	Third order natural frequency
Natural frequency value (Hz)	26.38	128.55	128.91
Main vibration modes	0	0.0278	-1
	-0.0001	-1	-0.0278
	1	-0.0007	0

Table 3 Natural frequency and vibration mode at random position

Order of natural frequency	First order natural frequency	Second order natural frequency	Third order natural frequency
Natural frequency value (Hz)	27.46	120.94	148.82
Main vibration modes	0.0678	-0.2417	-1
	0.0875	-1	0.2424
	1	0.0498	0.0234

ently. The first- and third-order natural frequencies increased, whereas the second-order natural frequencies decreased.

- (5) When the vibration frequencies were the first-, second-, and third-order natural frequencies, the maximum vibration responses appeared in the deflec-

tion, pitching, and rotation directions, respectively. Under actual operating conditions, the external excitation frequency is most likely to approach the first-order natural frequency; therefore, the mechanism is most prone to vibration in the deflection direction.

3.2 Natural Frequency Analysis in Workspace of Electro-hydraulic Driven 3-UPS/S Parallel Stabilization Platform

When the platform is used to maintain the stability of the horizontal direction of the equipment, the change range of the deflection angle is small, and the angle compensation is mainly performed through changes in the rotation and pitching directions. According to the workspace search theory, when the deflection angle is 28°, the change range of the pitch and rotating angles is the largest. Therefore, considering this position as the initial workspace, the natural frequency variation curve of the mechanism can be obtained as follows.

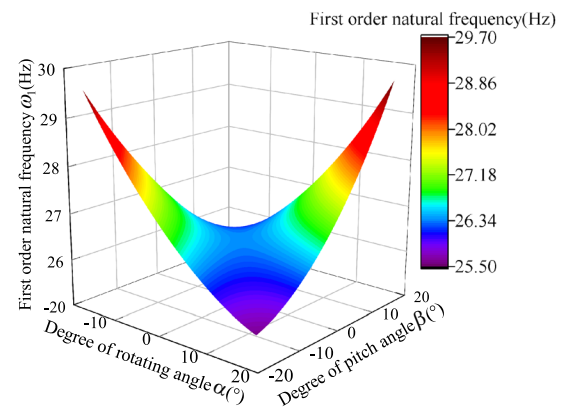
As shown in Figure 2, in the initial workspace, the natural frequencies of each order presented an obvious symmetry with the position change, and that for the first-order natural frequency was the most evident, corresponding to the movement in the deflection direction. When the mechanism gradually deviated from the initial position, the variation trends for the different orders of the natural frequencies were not the same. Meanwhile, the positions at which the maximum and minimum values of each order of the natural frequencies were obtained are different. In general, when the pitching angle is significantly different from the rotation angle, the natural frequency approaches its limit. However, the second-order natural frequency had a large value near the initial position. When the mechanism gradually deviated from the initial position through attitude compensation, the second-order natural frequency gradually decreased. In addition, the third-order of the natural frequency was the most sensitive to position changes, followed by the second-order of the natural frequency, and the first-order of the natural frequency was the least affected by position changes.

4 Force Vibration Analysis of Electro-hydraulic Driven 3-UPS/S Parallel Stabilization Platform

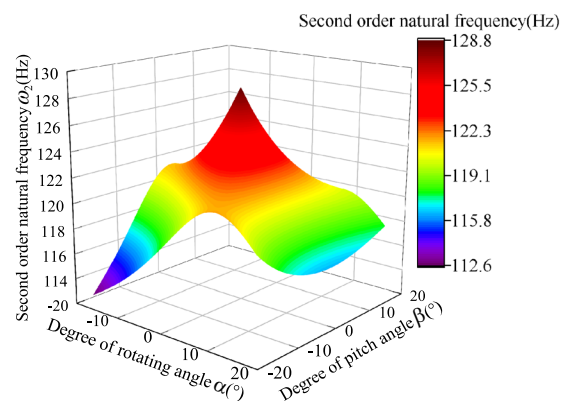
4.1 Vibration Response Analysis of Electro-hydraulic Driven 3-UPS/S Parallel Stabilization Platform

When the excitation frequency is close to the natural frequency of each order, the mechanism generates a resonance, which affects the compensation accuracy and control precision. Therefore, when the structural parameters remain unchanged, the vibration response of the mechanism at the random position $\alpha=10^\circ, \beta=10^\circ, \gamma=28^\circ$ is solved. The torque matrix acting on the mechanism is expressed as follows:

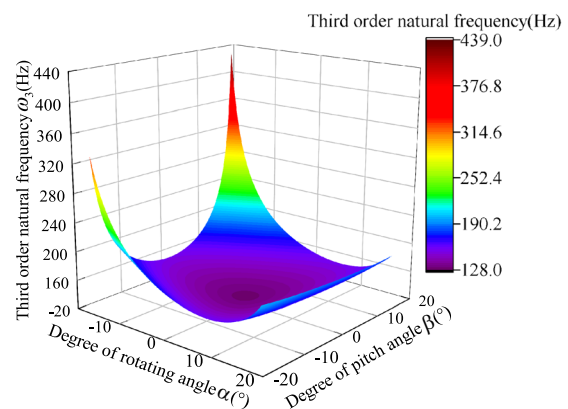
$$M_U = \begin{bmatrix} 80 \cos(\omega_0 t) \\ 80 \cos(\omega_0 t) \\ 80 \cos(\omega_0 t) \end{bmatrix}. \tag{31}$$



(a) Variation law for first-order natural frequency



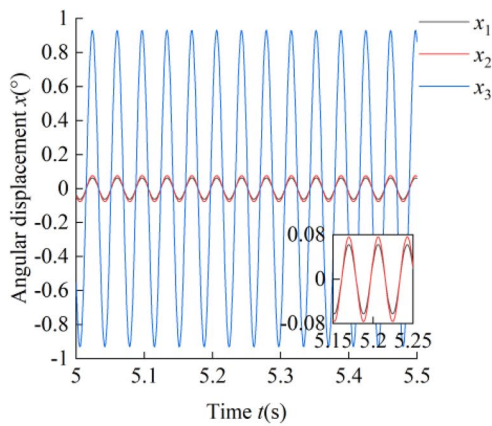
(b) Variation law for second-order natural frequency



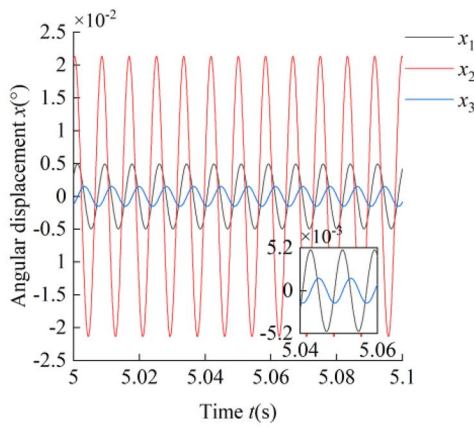
(c) Variation law for third-order natural frequency

Figure 2 Variation law for the natural frequencies in the initial workspace

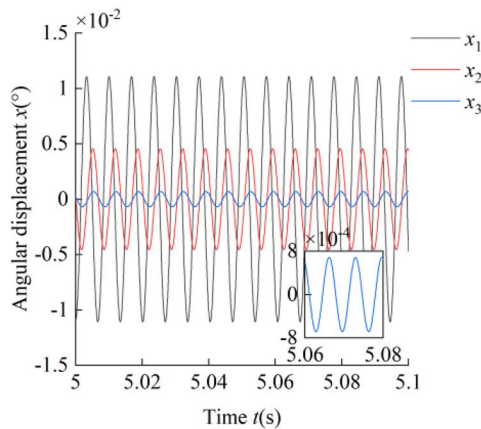
The time-domain curve of the vibration response is shown in Figure 3. As shown in Figure 3, when subjected to an external harmonic excitation whose frequency is close to the natural frequency, the mechanism generates



(a) Time domain response when $\omega_0 \approx \omega_1$



(b) Time domain response when $\omega_0 \approx \omega_2$



(c) Time domain response when $\omega_0 \approx \omega_3$

Figure 3 Time domain curves of forced vibrations

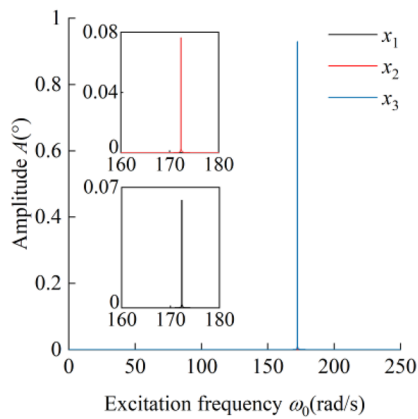
a resonance, and the steady-state response is a simple harmonic motion. When the excitation frequency was close to the first-, second-, or third-order natural frequencies, the angular displacement in the deflection, pitch, and rotation directions reached a maximum. When the external excitation frequency was close to the first-order natural frequency, the angular displacement of the mechanism in the rotation and pitching directions was approximately equal; however, when the angular displacement in the rotation or pitching directions reached the maximum, the angular displacement response in the other two directions was smaller, which is consistent with the main vibration mode.

The frequency-domain curve of the vibration response is shown in Figure 4. When the excitation frequency was close to the natural frequency of each order, the steady-state vibration response amplitude in each direction reached the maximum at the corresponding natural frequency. The maximum amplitudes of the vibration response were 0.932° in the deflection direction, 0.0213° in the pitching direction, and 0.0111° in the rotation direction. When the excitation frequency was close to the first-, second-, and third-order natural frequencies, the steady-state response amplitudes in each direction gradually decreased. When the excitation frequency was close to the first-order natural frequency, the steady-state vibration response in each direction was much larger than when the excitation frequency was close to the second- or third-order natural frequency. Thus, when the excitation frequency is close to the first-order natural frequency, the resulting resonance significantly influences the compensation and control accuracies.

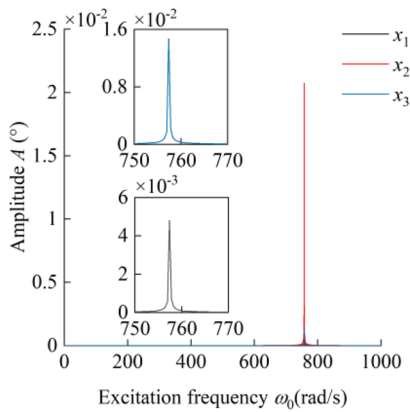
4.2 Vibration Response Amplitude Analysis in Workspace of Electro-hydraulic Driven 3-UPS/S Parallel Stabilization Platform

The amplitude of the vibration response was also related to the position of the mechanism. Therefore, by keeping the theoretical parameters unchanged, the vibration response amplitude in the initial working space was calculated for when the excitation frequency was close to the first-order natural frequency, and the results are shown in Figure 5.

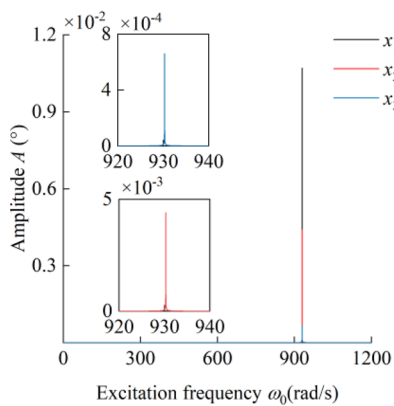
It can be seen from Figure 5 that when the excitation frequency is close to the first-order natural frequency, the amplitude curves of the vibration response in each direction show a certain symmetry, and that the locations at which the extreme values of the response amplitudes in each direction are obtained are not the same. In



(a) Frequency domain response when $\omega_0 \approx \omega_1$

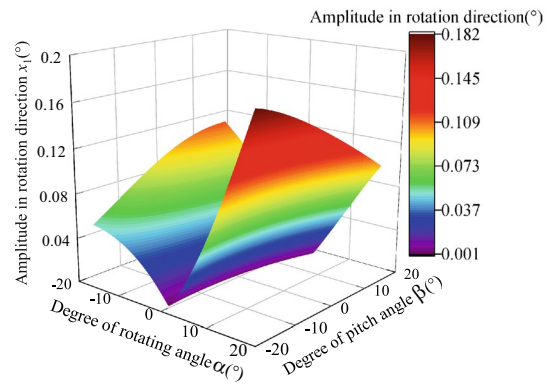


(b) Frequency domain response when $\omega_0 \approx \omega_2$

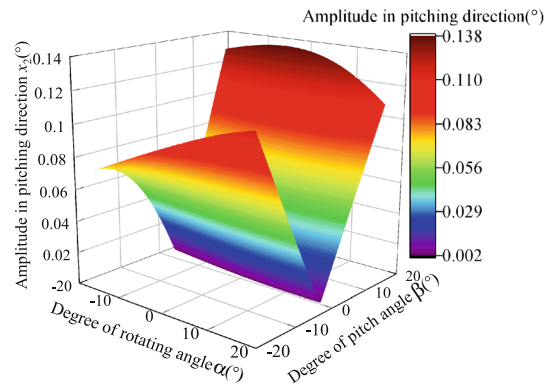


(c) Frequency domain response when $\omega_0 \approx \omega_3$

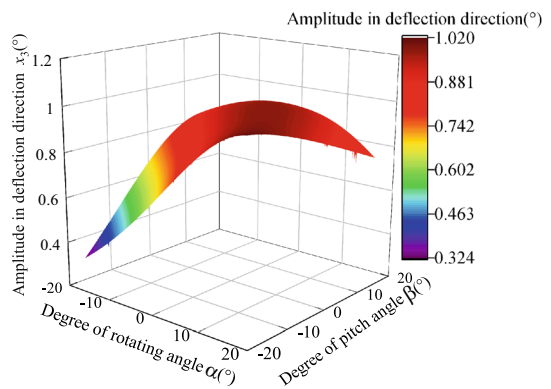
Figure 4 Frequency domain curves of forced vibrations



(a) Amplitude of vibration response in the rotation direction



(b) Amplitude of vibration response in the pitching direction



(c) Amplitude of vibration response in the deflection direction

Figure 5 Amplitudes of vibration response for $\omega_0 \approx \omega_1$

Figure 5(a), we show that the vibration response amplitude in the rotation direction was small when the pitch angle is approximately 0° . At this position, the vibration response amplitude in the rotational direction was insensitive to a position change in the pitching direction. Similarly, as shown in Figure 5(b), the vibration response amplitude in the pitch direction was relatively small when the pitch angle was approximately 0° . At this position, the vibration response amplitude in the pitch direction was insensitive to position changes in the rotation direction. When the mechanism gradually deviates from the initial position, the amplitude of the vibration response in the rotation and pitching directions gradually increases. When the difference between the rotation and pitch angles was large, the vibration response amplitudes in the rotation and pitching directions were large. As shown in Figure 5(c), when the position changed from the left to the right limit of the working space, the amplitude of the vibration response in the deflection direction increased gradually. When the excitation frequency was close to the first-order natural frequency, the vibration response amplitude in the deflection direction was much larger than those in the pitch and rotation directions, and the maximum value was greater than 1° . The vibration generated by the mechanism has a significant impact on the control accuracy.

5 Verification of Dynamic Theoretical Model of Electro-hydraulic Driven 3-UPS/S Parallel Stabilization Platform

5.1 Verification of Theoretical Free Vibration Model

To verify the correctness of the theoretical free vibration model, the natural frequency of the prototype was measured at the random position $\alpha=10^\circ$, $\beta=10^\circ$, $\gamma=28^\circ$

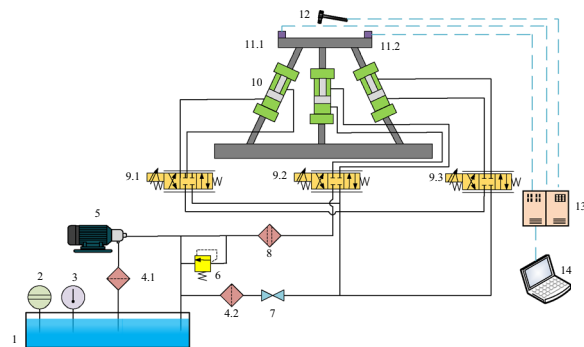


Figure 6 Schematic diagram of modal experiment. 1–oil tank, 2–liquid level gauge, 3–liquid temperature gauge, 4–filter, 5–motor pump, 6–overflow valve, 7–check valve, 8–filter, 9–servo valve, 10–electro-hydraulic driven 3-UPS/S parallel stabilization platform prototype, 11–acceleration sensor, 12–force hammer, 13–lower computer, 14–computer

using the pulse excitation method. A schematic of the experimental setup is shown in Figure 6. A force hammer strikes the moving platform to generate an impulse excitation force. The signal of the exciting force then enters the lower computer through the force sensor and voltage amplifier on the force hammer. The axial response signal of the prototype is collected by the acceleration sensor and input to the computer through the voltage amplifier and lower computer. The experimental prototype and test diagram are shown in Figures 7 and 8, respectively.

The sampling frequency used in the experiment was 640 Hz; therefore, it met the sampling theorem, and the collected signals were reliable. The time-domain curves of the excitation and vibration signals collected during the experiment are presented in Figure 9.

After processing the data shown in Figure 9, the spectral power density curve of the prototype response signal was obtained, as shown in Figure 10. The curve exhibited peaks at 26.31 Hz, 126.41 Hz and 141.88 Hz. A comparison of the theoretical and experimental values of the natural frequency is shown in Table 4. The maximum error between the theoretical and experimental values is 4.66%, which verifies the correctness of the theoretical model.

5.2 Verification of Theoretical Forced Vibration Model

To verify the correctness of the theoretical forced vibration model of the mechanism, and taking the excitation frequency close to the first-order natural frequency as example, the fourth-order Runge-Kutta method was used to solve the time-domain and frequency-domain characteristic curves of the vibration response, and the results are shown in Figure 11.

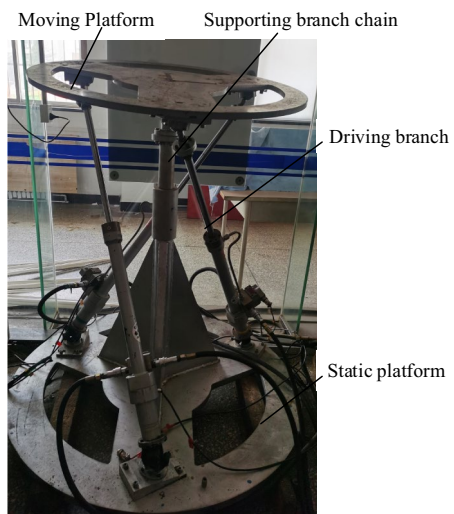
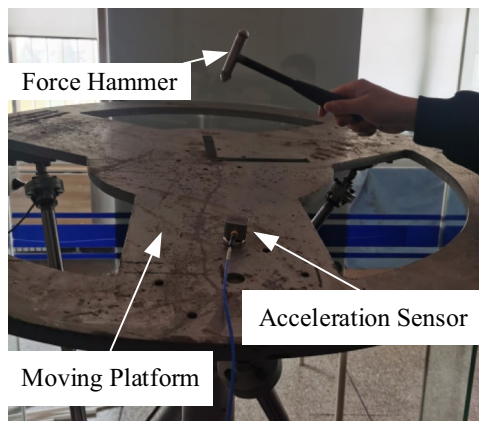
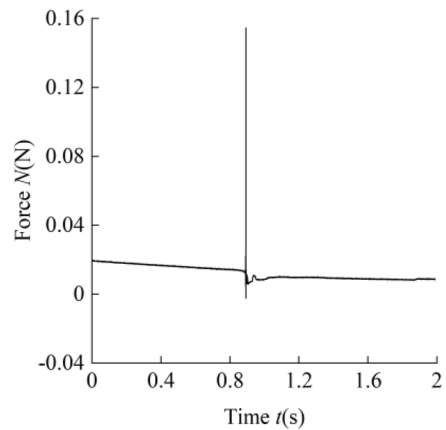


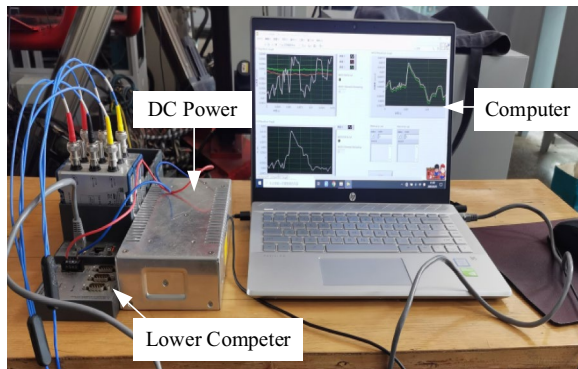
Figure 7 Electro-hydraulic drive 3-UPS/S parallel stabilization platform prototype



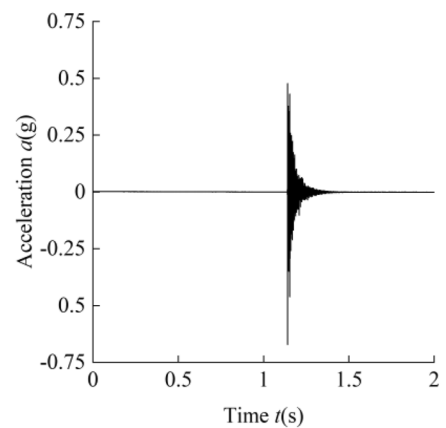
(a) Modal test platform



(a) Excitation signal of the system



(b) Signal acquisition and analysis system



(b) Acceleration response of the system

Figure 8 Modal test diagram

Figure 9 Time domain curve of the measured signal

As shown in Figure 11(a), when the excitation frequency is close to the first-order natural frequency, the time-domain curve of the numerical solution exhibits a stable simple harmonic motion, which is consistent with the results of the theoretical analysis. By comparing Figures 3(b) and 11(b), it can be seen that the numerical solutions of the maximum vibration response amplitude in the rotation, pitching, and deflection directions were 0.0627° , 0.0766° and 0.932° respectively. Correspondingly, the maximum vibration response amplitudes obtained from the theoretical calculations in each direction were 0.0626° , 0.0765° and 0.9316° , respectively. A comparison between the theoretical and numerical values of the maximum vibration response amplitude is shown in Table 5; the maximum error between the theoretical and numerical solutions is 0.16%, which verifies the correctness of the theoretical forced vibration model.

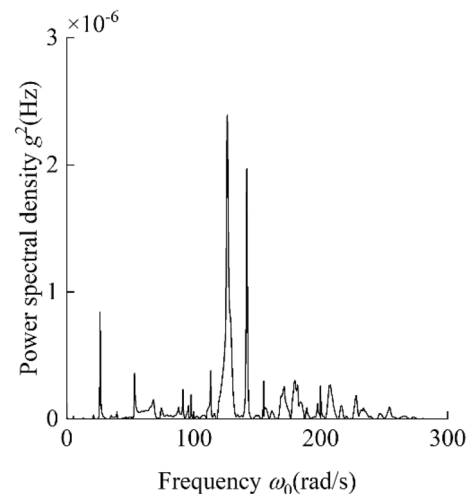
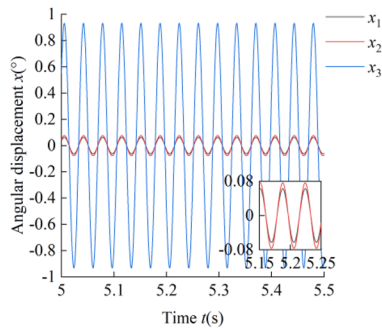


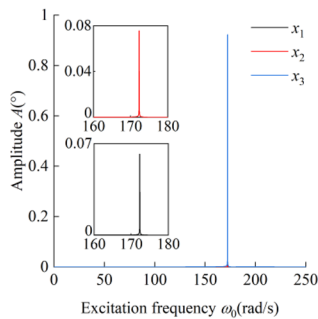
Figure 10 Power spectral density of the system response

Table 4 Comparison of theoretical and experimental values of the natural frequency

Experimental result	Theoretical value (Hz)	Experimental value (Hz)	Error (%)
First order natural frequency	27.46	26.31	4.18
Second order natural frequency	120.94	126.41	4.5
Third order natural frequency	148.82	141.88	4.66



(a) Time domain curve of numerical solution



(b) Frequency domain curve of numerical solution

Figure 11 Time domain curve of steady-state response numerical solution

Table 5 Comparison of theoretical and numerical values of maximum vibration response amplitude

Direction	Theoretical value (°)	Numerical value (°)	Error (%)
Rotation direction	0.0627	0.0626	0.16
Pitching direction	0.0766	0.0765	0.13
Deflection direction	0.932	0.9316	0.042

6 Conclusions

- (1) The natural frequency is a function of the position of the mechanism. In the initial working space, the change in the natural frequency was symmetrical,

and the position for obtaining the extreme value was not the same. With a change in position, the third-order natural frequency changed the most, followed by the second-order natural frequency, and the first-order natural frequency changed the least.

- (2) When the mechanism resonated with the external excitation of a simple harmonic motion, the steady-state resonance response presented a simple harmonic motion. When the excitation frequency was close to the first-, second-, and third-order natural frequencies, the amplitude of the vibration response reached a maximum in the deflection, pitching, and rotation directions, respectively.
- (3) The vibration response amplitude varied symmetrically in the initial working space. When the excitation frequency was close to the first-order natural frequency, the vibration response amplitude in the deflection direction was larger than that in the other two directions, and the value was close to 1°, which had a significant influence on the compensation and control accuracies.
- (4) A modal test and fourth-order Runge-Kutta numerical simulation were used to verify the theoretical model. The maximum error between the theoretical and experimental values was 4.66%, and the maximum error between the numerical and theoretical values was 0.16%, verifying the correctness of the theoretical model.

Acknowledgements

Not applicable.

Authors' Contributions

XY and LZ were in charge of the entire trial; WW wrote the manuscript; and HP assisted with the sampling and laboratory analyses. All authors read and approved the final manuscript.

Funding

Supported by National Key Research and Development Program of China (Grant No. 2019YFB2005303), General Fund of the National Natural Science Foundation of China (Grant No. 52175066), Hebei Provincial Natural Science Foundation of China (Grant No. E2020203090), and Hebei Provincial Key Science and Technology Projects in the Colleges and Universities of China (Grant No. ZD2022052).

Data availability

All relevant data are within the paper.

Declarations

Competing Interests

The authors declare no competing financial interests.

Received: 24 March 2023 Revised: 8 July 2024 Accepted: 22 July 2024
Published online: 26 August 2024

References

- [1] Y C Wang, Y M Yang, H P Kuang. High performance both in low-speed tracking and large-angle swing scanning based on adaptive nonsingular fast terminal sliding mode control for a three-axis universal inertially stabilization platform. *Sensors*, 2020, 20(20): 16–18.
- [2] X Y Zhou, Y Jia, Y Li Y. An integral sliding mode controller based disturbances rejection compound scheme for inertially stabilization platform in aerial remote sensing. *Proceedings of the Institution of Mechanical Engineers*, 2018, 232(5): 26–27.
- [3] S Q Wang, X G Li, Z Q Mei, et al. Motion analysis and control system design of 3DOF WAVE simulator. *Journal of Mechanical & Electrical Engineering*, 2020, 37(2): 201–205.
- [4] M Y Zhang, Y L Guan, W W Zhao. Adaptive super-twisting sliding mode control for stabilization platform of laser seeker based on extended state observer. *Optik*, 2019, 12(33): 199–201.
- [5] J M Hilkert. Inertially stabilization platform technology concepts and principles. *IEEE Control Systems Magazine*, 2008, 28(1): 26–46.
- [6] L L Wang, J Z Xiao, H Wang, et al. Development of a parallel-series stabilization platform system. *Applied Mechanics and Materials*, 2013, 319: 414–418.
- [7] J F Wen, G Wang, J C Jia, et al. Compliance control method for robot joint with variable stiffness. *International Journal of Hydromechanics*, 2023, 6(1): 45–48.
- [8] M Zhai, T Yang, N Sun, et al. Observer-based adaptive fuzzy control of under-actuated offshore cranes for cargo stabilization with respect to ship decks. *Mechanism and Machine Theory*, 2022, 175: 104987.
- [9] S A A Shah, B T Gao, A K Bhatia, et al. Anti-vibration control design for TORA based barge-type offshore floating wind turbine using extended order high gain observer. *Engineering Computations*, 2022, 39(7): 2705–2732.
- [10] A Morinaga, T Ogawa, K Iwanaga, et al. Development of motion reduction device for ship using underactuated parallel link mechanism. *Sensors and Materials: An International Journal on Sensor Technology*, 2021, 33(3): 897–906.
- [11] W J Liu, J L Du, J Li, et al. Stabilization control of 3-DOF parallel vessel-borne platform with dynamic uncertainties and unknown disturbances. *Applied Ocean Research*, 2022, 126(21): 1–11.
- [12] J Zhang, J Y Li, T Wang, et al. Influence of nozzle structure on the flow field of the prestage of nozzle flapper servo valve. *International Journal of Hydromechanics*, 2023, 6(1): 59–75.
- [13] W Hunek, P Majewski, J Zygarlicki, et al. A measurement-aided control system for stabilization of the real-life Stewart platform. *Sensors*, 2022, 22(19): 7271.
- [14] J C Mi, G Q Huang. Dynamic prediction of performance degradation characteristics of direct-drive electro-hydraulic servo valves. *Applied Sciences-Basel*, 2023, 13(12): 7231.
- [15] X M Yuan, W W Wang, X Zhu, et al. Theoretical model of dynamic bulk modulus for aerated hydraulic fluid. *Chinese Journal of Mechanical Engineering*, 2022, 35: 121.
- [16] S Solaichari, J Lakshminpathy. Vibration control of an unbalanced system using a quasi-zero stiffness vibration isolator with fluidic actuators and composite material: An experimental study. *Journal of Vibration and Control*, 2023, 29(3): 688–699.
- [17] X D Jia, S Wang, X Q Yan, et al. Research on dynamic response of cold rolling mill with dynamic stiffness compensation. *Electronics*, 2023, 12(3): 599.
- [18] X J Yang, B F Song, J L Xuan. Effects of the mechanical vibrations on the thrust force characteristics for the PMLM driven motion system. *Mechanical Systems and Signal Processing*, 2022, 175: 109110.
- [19] X M Yuan, W Q Wang, X Zhu, et al. Analysis of free vibration of hydraulic opposing cylinder controlled by servo valve. *Transactions of the Canadian Society for Mechanical Engineering*, 2022, 46: 651–667.
- [20] X M Yuan, W Q Wang, X Zhu, et al. Analysis of parametric vibration of hydraulic opposing cylinder controlled by servo valve considering pressure pulsation. *Transactions of the Canadian Society for Mechanical Engineering*, 2022, 46: 668–684.
- [21] H L Yang, Q Chen, H F Liu, et al. Investigation on distributed vibration damping of bridge based on energy harvesting technique and finite element analysis. *Applied Sciences-Basel*, 2023, 13(1): 382.
- [22] Z W Cao, G Yao. Parametric vibration stability analysis of a pyramid lattice sandwich plate subjected to pulsatile external airflow. *Acta Mechanica Solida Sinica*, 2023, 36(1): 95–104.
- [23] Y C Zhu, S K Au. Bayesian data driven model for uncertain modal properties identified from operational modal analysis. *Mechanical Systems and Signal Processing*, 2020, 136: 1–24.
- [24] C O Zhi, C T Hong, A Brandt, et al. An inconsistent phase selection assessment for harmonic peaks elimination in operational modal testing. *Archive of Applied Mechanics*, 2019, 89(12): 2415–2430.
- [25] J H Yang, H F Lam, L B James. Bayes-Mode-ID: A Bayesian modal-component-sampling method for operational modal analysis. *Engineering Structures*, 2019, 189: 222–240.
- [26] H Chen, C H Lu, Z E Liu, et al. Structural modal analysis and optimization of SUV door based on response surface method. *Shock and Vibration*, 2020: 9362434.
- [27] P G Golano, L Z Fragonara, P Morantz, et al. Numerical and experimental modal analysis applied to an optical test system designed for the form measurements of metre-scale optics. *Shock and Vibration*, 2018: 3435249.
- [28] Y Yasa, Y Sozer, M Garip. Acoustic noise mitigation of switched reluctance machines with leaf springs. *IEEE Transactions on Industrial Electronics*, 2022, 70(2): 1250–1260.
- [29] X Yang, Y S Wang, Z Y Zhang, et al. Simulation and experimental analysis on frictional vibration in the reversal process of a wiper-windscreen system. *Applied Acoustics*, 2023, 203: 109211.
- [30] M Dumitriu, T Mazilu, I I Apostol. Scale models to verify the effectiveness of the methods for reducing the vertical bending vibration of the railway vehicles carbody: Applications and design elements. *Applied Sciences-Basel*, 2023, 13(4): 2368.
- [31] Z F Bin, Z C Ong, S Y Khoo. A review of operational modal analysis techniques for in-service modal identification. *Journal of the Brazilian Society of Mechanical Sciences and Engineering*, 2020, 42(8): 398.
- [32] F Ebrahimi, E Salari. Thermal buckling and free vibration analysis of size dependent Timoshenko FG nanobeams in thermal environments. *Composite Structures*, 2015, 128: 363–380.
- [33] A A Hanieh, A Preumont. Multi-axis vibration isolation using different active techniques of frequency reduction. *Journal of Vibration & Control*, 2011, 17(5): 759–768.
- [34] Y K Li, Y Q Li, Y X Wan, et al. Analysis of 3-UPS/S parallel platform vibration responses under hydraulic servo drives. *China Mechanical Engineering*, 2019, 30(4): 423–430.
- [35] M Yang, S L Xiao, Y Yuan. Controller design and experimental investigation of a 3-universal-prismatic-universal compliant manipulator for active vibration isolation. *Journal of Vibration and Control*, 2015, 21(16): 3218–3238.

Xiaoming Yuan born in 1984, is currently an associate professor at *Yanshan University, China*. He received his Ph.D. degree from *Yanshan University, China*, in 2014. His research interests include the fluid-structure interaction dynamics of firefighting monitors, fluid transmission and control, and new magnetic gear transmission and control.

WeiQi Wang received the B.S. degree from *School of Mechanical Engineering, Yanshan University, China*, in 2020, where he is currently pursuing the Master's degree. His research interests include fluid transmission and control.

Haodong Pang born in 1998, received the B.S. degree from *School of Mechanical Engineering, Nanjing Normal University Zhongbei College, China*, in 2020. He is currently pursuing a Master's degree at *Yanshan University, China*. His research interests include fluids and electromagnetic transmissions.

Lijie Zhang born in 1969, is currently the vice president of *Hebei Agricultural University, China*. He received his Ph.D. degree from *Yanshan University, China*, in 2006. His research interests include the reliability and fault diagnosis of hydraulic components, multiphysics coupling analysis, mechanics, and robotics.